Journal of Physics: Conference Series **3054** (2025) 012034 doi:10.1088/1742-6596/3054/1/012034

Experimental characterization of the axial rotational instability of the cryogenic rotation mechanism using synchronous motor and superconducting magnetic bearing

Taisei Iwagaki[1], Kosuke Aizawa[1], Ryosuke Akizawa[1], Gilberto Goracci[2], Teruhito Iida[3], Tomotake Matsumura[4,5,6,7], Jun Nakagawa[4], Hiroyuki Ohsaki[8], Satsuki Okumura[8], Yuki Sakurai[4,9], Sherry Song[4], Ryota Takaku[10] and Yutaka Terao[8]

[1]Department of Physics, The University of Tokyo, Tokyo, Japan
[2]Dipartimento di Fisica, Universit'a di Roma Tor Vergata, Via della Ricerca Scientifica 1, Roma, Italy
[3]task inc., Suginami, Tokyo, Japan
[4]Kavli Institute for the Physics and Mathematics of the Universe (WPI), The University of Tokyo, Kashiwa, Chiba, Japan
[5]Center for Data Driven Discovery (CD3), Kavli Institute for the Physics and Mathematics of the Universe (WPI), The University of Tokyo, Kashiwa, Chiba, Japan
[6]ILANCE, CNRS, University of Tokyo International Laboratory, Chiba, Japan
[7]Institute of Space and Astronautical Science (ISAS), Japan Aerospace Exploration Agency (JAXA), Sagamihara, Kanagawa, Japan
[8]Graduate School of Frontier Sciences, The University of Tokyo, Kashiwa, Chiba, Japan
[9]Suwa University of Science, Chino, Nagano, Japan
[10]Inter-University Research Institute Cooperation High Accelerator Research Organization (KEK), International Center for Quantum-field Measurement Systems for Studies of the Universe and Particles (QUP), Tsukuba, Ibaraki, Japan

E-mail: taisei.iwagaki@ipmu.jp

Abstract. We report the experimental characterization of the rotational instability of a cryogenic rotation mechanism, which uses a superconducting magnetic bearing (SMB) and a synchronous motor and operates at about 10 K in a vacuum environment. We conducted rotation tests: driving the rotor and reconstructing the rotational frequency of the rotor. We identified the rotational frequency oscillations and the damping of its amplitude around the target rotational frequency set by the motor drive electronics. The amplitude of the oscillation of about 0.005 Hz at the rotational frequency of 0.77 Hz with the damping coefficient of about 0.02 s^{-1}. We compared this damping coefficient to the energy loss by the rotational frequency spin down without any driving torque. We found that the two damping coefficients agree within a factor of two. Based on the analysis, we narrowed down the cause of the oscillation to the low-torque/low-friction rotation mechanism together with the high-purity copper wires used in drive motor coils as the source of eddy current.

1 Introduction

A superconducting magnetic bearing (SMB) has great potential in applications of low-energy loss systems. A typical SMB consists of a ring-shaped permanent magnet as a rotor that levitates over the high-temperature superconductor (HTS) array as a stator, cooled below its critical temperature. We employ YBCO, a Type-II superconductor, used for SMB that pins the flux when it is cooled with the external magnetic field, so-called field-cooling. When the magnetic field of the rotor magnet has rotational symmetry about the axis of rotation, the HTS does not experience the change in the applied magnetic field [1]. Thus, the rotor ring magnet rotates freely without any physical contact. This attractive feature enables us to construct a bearing with no mechanical contact and, thus, no physical friction. As a result, SMB achieves low energy loss, and is capable of operating in low-temperature and vacuum environments, e.g., energy-storage flywheels [2, 3], sensitive gravimeters [4], micro-force measurement [5], lunar telescopes [6], and polarimeters [7, 8].

One application of SMB that drives operating below 77 K is for the rotation mechanism of the cosmic microwave background (CMB) polarimeter. The limited cooling power of a telescope cryogenic system and the need for the cryogenically cooled optical element to minimize the heat dissipation from the polarimeter. Thus, these demands lead to the use of SMB-based rotation mechanisms. The balloon-born [9] and several ground-based CMB telescopes have implemented a polarimeter using SMB [10, 11].

This attractive low-friction feature becomes a trade-off to the low-damping to any undesirable oscillatory natures in its rotational kinetics. The oscillation can happen in any degree of freedom. SMB constrains the oscillation in the axial, radial, and tilt directions, and the oscillatory amplitude depends on the external force and effective spring constant in each axis. The oscillation in the rotational direction is not constrained due to the rotational symmetric magnetic field. When the rotor is driven by the drive mechanism, e.g., the motor, the torque can be a source of an external force in the rotational axis, and its strength determines the constraint in the rotational degree of freedom. When the drive mechanism rotates the rotor by circulating current through coils to synchronize the rotating magnetic field with that of the rotor magnets, the current can be another source of energy loss via Joule heat. As a result, it is motivated to reduce the drive current, leading to low coupling torque between the rotor and the stator and the potential oscillation in the axial direction. This oscillation does not damp out if the levitation system contains no energy loss. Thus, there is a trade-off between the two conflicting effects as we pursue the realization of both no energy loss and no oscillation.

In this paper, we report the measurements, results, and physical interpretation of the rotational instability of the cryogenic rotation mechanism supported by the SMB. Section 2 outlines the setup of the cryogenic rotation mechanism. Section 3 describes the methods of the rotation measurements and the analysis of the rotational frequency. Section 4 presents the result of the rotational instability, and the physical interpretation of the rotational instability and its damping follows in Section 5.

2 Overview of the rotation mechanism

We designed and fabricated the rotation mechanism operating at the cryogenic temperature [12]. Tab. 1 lists the design specifications of the rotation mechanism. This design is motivated for the performance demonstration of the rotation mechanism of a space millimeter-wave polarimeter[7, 8]. Fig. 1 shows a photograph and a cross-section of a 3D-CAD model. This rotation mechanism consists of an SMB, a synchronous motor as a drive mechanism, optical encoders, and cryogenic holder mechanisms. There is a hole in the middle of this rotation mechanism to mount an optical element for the polarimeter.

The SMB consists of the 32 samarium-cobalt (SmCo) permanent magnets as a rotor and the 46 bulk YBCO arrays as a stator. YBCO is a type-II superconductor that pins the magnetic flux when it is cooled below the critical temperature of approximately 95 K. Once it is cooled down, the frozen magnetic field will achieve the stable levitation of the rotor ring. The rotor magnets and YBCO arrays are ring-shaped to construct the hollow rotation mechanism for mounting an optical system as a polarimeter. The SmCo magnets of the rotor are radially magnetized, and the magnetic circuit is assembled with ring-shaped magnetic yokes. This magnetic circuit optimizes the magnetic flux lines and minimizes the magnetic field inhomogeneities.

The drive mechanism is based on a synchronous motor consisting of 72 SmCo magnets aligned with alternating poles on the rotor and 18 sets of three-phase coils on the stator. We use 54 coreless coils, each consisting of 24 turns with 6N high-purity copper wire with a diameter of 0.5 mm. We employ high-purity copper specifically to reduce the Joule heat. At the cryogenic temperature below 10 K, the electrical resistance of this copper wire is about 1/20 that of a typical copper magnet wire [13, 14]. More specifically, RRR, which is defined as the ratio of resistivity at temperatures 273 K and 4 K: RRR $= \rho(273\ \mathrm{K})/\rho(4\ \mathrm{K})$, is about 2000. This motor makes the rotating magnetic field by a three-phase current shifted by 120 degrees flowing through the coils on the stator. The rotor rotates while

synchronizing with the magnetic field of the magnets and the rotating magnetic field.

To measure the rotational frequency, we employ an incremental optical encoder. This encoder consists of an aluminum encoder disk as an optical chopper attached on the rotor and three pairs of LEDs (Hamamatsu model# L7558-01) and silicon photodiodes (Hamamatsu model# S2386-18L) mounted on the stator. The encoder disk has 128 slots at the outer radius to monitor the rotational angle and one slot at the inner radius to set an initial position of the rotation. Each slot at the outer radius corresponds to an angular resolution of $360/128 \sim 2.8$ deg. The rotational frequency is reconstructed using the voltage signal from the photodiodes. The reconstruction algorithm is described in the following section. We employ two sets of encoders, each containing three pairs of LEDs and photodiodes, named phase A, phase B, and phase Z, respectively. The right image of Fig. 1 shows the relative position of A, B, and Z. The phase Z monitors the slot at the inner radius and receives one signal per revolution. Both phase A and B read the 128 slots at the outer radius. The output signals from A and B are shifted by 1/4 of one period.

Table 1: The design specifications of the rotation mechanism [12]

Parameter	Design specification
Diameter (Half wave plate)	480 mm
The operating temperature	5 K
The total heat dissipation	$\leq$ 4 mW
The rotation frequency	0.77 Hz

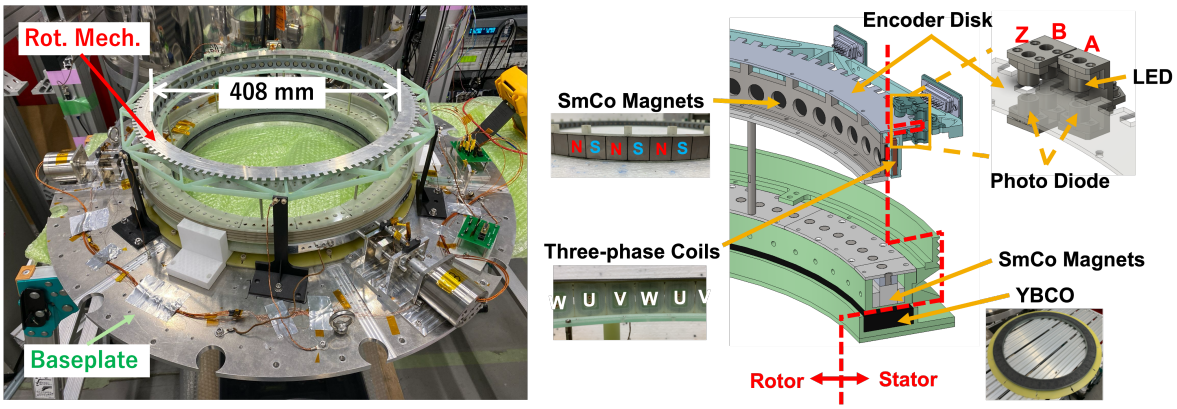

Figure 1: The overview of the cryogenic rotation mechanism (left) and the cross-section of the 3D-CAD model (right).

3 Experiments

In this section, we describe the experimental setup and the experimental procedures.

3.1 Experimental setup

The cryogenic rotation mechanism is placed inside a custom-built cryostat and cooled down by a two-stage Gifford-McMahon (GM) cooler. We monitored the change of temperature using diode thermometer (Lakeshore part# DT-670) at baseplate and a resistor based thermometer (Cernox) at near the GFRP coil bobbin on the stator. Each optical encoder monitors the slots on the encoder disk. The LEDs are biased by a current source, applying 80 μA to minimize the heat dissipation from the LEDs in a cryogenic environment. The voltage signals from the photodiodes are read by A/D converters (National Instruments NI-USB 9215) from outside the cryostat via feedthrough and stored by a computer.

3.2 Rotation tests

We conducted rotation tests with the entire rotation mechanism placed in the cryostat, and the entire system was first kept at about 10 K. The motor controller drove the rotor at a target frequency of 0.77 Hz, with an acceleration rate increasing by 0.0056 Hz every 20 seconds. The rotor then reached a constant rotational frequency of about 0.77 Hz. After approximately 10 minutes of the constant rotation, we conducted a spin-down test by disconnecting the motor controller and allowing the rotor to decelerate freely. Seven rotation tests were performed during cryostat warming at different initial coil temperatures, ranging from 37 K to 63 K at the coil bobbin. The panel of Fig. 2 shows an example of the rotational frequency and corresponding temperature of the baseplate and the stator near the coil bobbin. The baseplate is the bottom part of the mechanism as shown in the left image of Fig. 1.

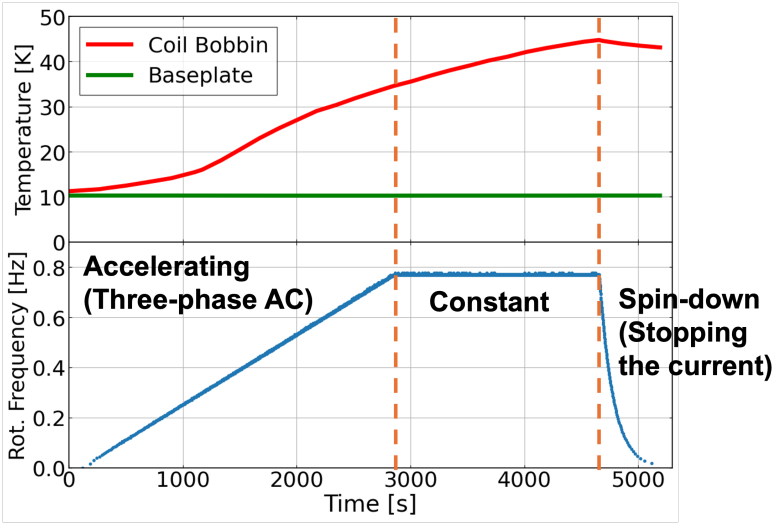

Figure 2: Rotational frequency during a rotation test (bottom) and corresponding temperature of the baseplate and coil bobbin (top).

3.3 Reconstruction of rotational frequency

The rotational frequency is reconstructed by the voltage measured by the optical encoder B, which read 128 slots of the encoder disk. The blue line in the graph of Fig. 3 shows the measured voltage signal of the phase B. Note that the signal has a DC offset at the baseline approximately 1.085 V, because the photodiode is measured using a single-ended measurement as a floating source. The signal drops below the baseline when the LED light passes through the slots. We estimate the rotational frequency by analyzing the signal using an algorithm described below. First, the algorithm sets the threshold at 1.067 V, as represented by the orange horizontal line in Fig. 3. Second, when the signal drops below the threshold, the estimated time t_n of this event is calculated using linear interpolation between the two data points immediately before and after the threshold crossing. A total of 128 estimated time points are stored during a single rotation and the algorithm calculates intervals between each point, denoted as $\Delta t_n = t_{n+1} - t_n$. Finally, we convert the intervals into the rotational frequency calculated by $f = \dfrac{1}{128\Delta t_n} = \dfrac{1}{128(t_{n+1} - t_n)}$.

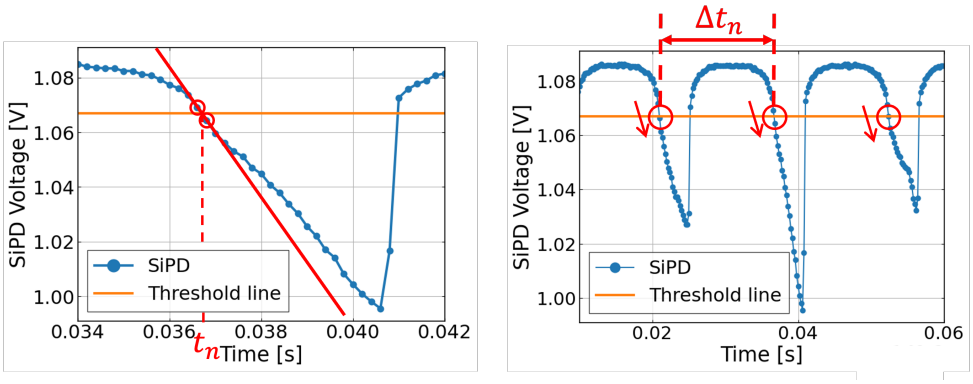

Figure 3: How to estimate the time of signals t_n (left). How to calculate the intervals between each signal (right). The blue line is the measured voltage of the encoder B, the orange horizontal line is the threshold at 1.067 V, and the red straight line is connecting two data points immediately before and after the threshold crossing.

4 Results

4.1 Axial rotational instability

Fig. 4 shows an example of the reconstructed rotational frequency and the corresponding zoom-in plot at constant rotation, with the target frequency of 0.77 Hz shown as a black line. We found that the reconstructed rotational frequency oscillates around the target frequency and the oscillation slightly damped over time. We define these damped oscillation features around the target frequency as the axial rotational instability in this paper.

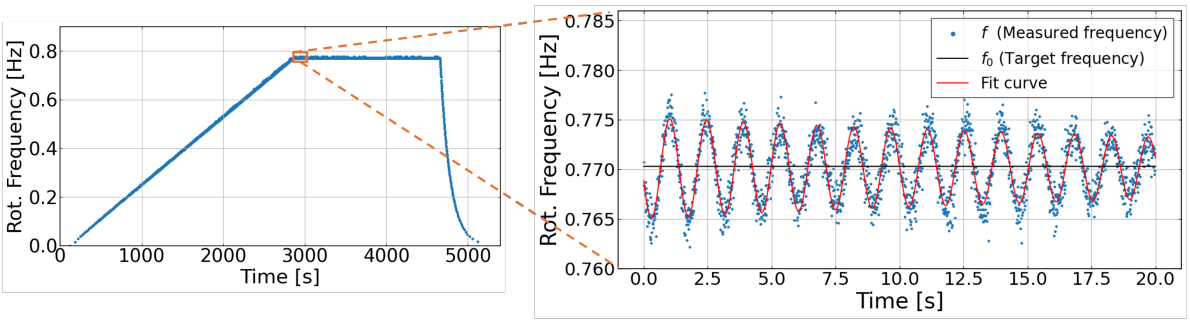

Figure 4: Reconstructed rotational frequency during a rotation test (left) and the zoom-in plot at the start of constant rotation (right). The blue points show the reconstructed rotational frequency, the black horizontal line is the target frequency of about 0.77 Hz, and the red line is the fit curve using the Eq. (2).

4.2 Quantification of the rotational instability

To quantify the axial rotational instability, we introduce a model coming from classical mechanics to represent the damped oscillation. Generally, the amplitude of oscillation in weakly damping system is given by

$$\frac{d^2(\Delta f)}{dt^2} + 2\gamma \frac{d(\Delta f)}{dt} + \omega_0^2 \Delta f = 0, \tag{1}$$

where Δf is the difference between the reconstructed rotational frequency and the target frequency, γ is the damping coefficient and ω_0 is the undamped angular frequency respectively. The solution of the equation can be written as

$$\Delta f = \Delta f_0 e^{-\gamma t} \cos(\omega t + \theta), \tag{2}$$

where Δf_0 is the initial amplitude, $\omega = \sqrt{\omega_0^2 - \gamma^2}$, and θ is the initial phase. We fitted the reconstructed rotational frequency using Eq. (2) to characterize 2γ as the damping coefficient, as shown in Fig. 4. We performed seven rotation tests at different coil temperatures, ranging from 37 K to 63 K, at the coil bobbin during cryostat warming. The corresponding 2γ values were determined by fitting the data from the first 20 seconds of constant rotation for each temperature. Δf_0 varies from 0.002 to 0.009 Hz at the rotational frequency of 0.77 Hz with the γ of about 0.01 to 0.04 s^{-1}. Fig. 5 shows the damping coefficients as a function of coil bobbin temperature, and we identified 2γ decreases as the coil bobbin temperature increases.

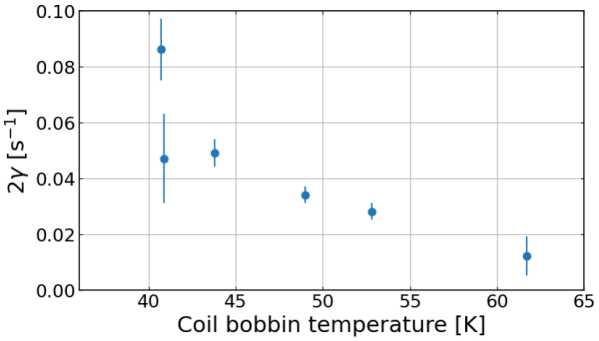

Figure 5: The damping coefficient 2γ as a function of coil bobbin temperature.

4.3 Energy loss estimation using spin-down data

The damping coefficients, 2γ, can be interpreted as the energy loss in the system. To confirm this relation, we estimated the total energy loss independently from the spin-down test shown at $t > 4700$ seconds in Fig. 2. At the spin-down period, the rotor loses its rotational energy. This is a common method to estimate the energy loss in the SMB-based rotational system [14, 15]. The physical origins of the loss are identified as hysteresis and eddy current from the SMB itself and its neighbor structures, in our case, the SMB and the drive mechanism. The deceleration of the rotor can be modeled by the following equation,

$$\frac{df(t)}{dt} = -\frac{a_0}{2\pi} - a_1 f(t), \tag{3}$$

where a_0 and a_1 are the coefficients of the hysteresis and eddy current loss, respectively. These coefficients contain the effects of both the SMB and drive mechanism because these two effects cannot be separated. The solution of this equation can be written as

$$f(t) = -\frac{a_0}{2\pi a_1} + \left(\frac{a_0}{2\pi a_1} + 2\pi f(t_0)\right) e^{-a_1(t-t_0)}, \tag{4}$$

where t_0 is the time when the spin-down starts. The left panel of Fig. 6 is an example of the spin-down profile at 41.5 K and fit curve using Eq. (4). Tab. 2 summarizes the parameters obtained at different coil temperatures. We identified that a_1 is more than 10 times larger than a_0, indicating that the eddy current loss is dominant in the deceleration.

Table 2: The estimated parameters a_0 and a_1 at different coil temperatures of the spin-down profile.

Temperature [K]	$a_0 \times 10^{-4}$ [s^{-2}]	$a_1 \times 10^{-4}$ [s^{-1}]
36.9	16.0 ± 1.3	580.5 ± 0.9
41.5	15.31 ± 0.13	347.2 ± 0.8
42.6	13.2 ± 1.2	313.5 ± 0.7
50.0	4.40 ± 0.05	175.4 ± 0.2
51.6	5.39 ± 0.04	160.63 ± 0.17
56.5	3.27 ± 0.02	116.951 ± 0.010
63.3	2.846 ± 0.012	82.259 ± 0.006

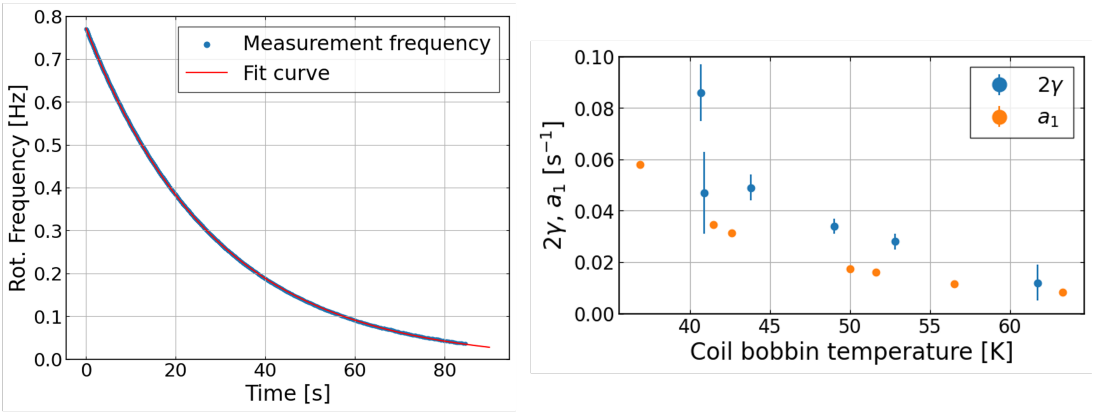

Figure 6: The spin-down profile with the fit curve (left). The comparison between the damping coefficient 2γ and the eddy current coefficient a_1 from the spin-down as a function of coil bobbin temperature (right). Note that the two data points for 2γ at the coil temperature of around 41 K are taken during the GM cooler *on* while the other data points for 2γ are taken with the GM cooler *off*.

5 Discussions

5.1 The origin of energy loss

We measured both the damping and the eddy current coefficients, and compared them as a function of temperature. The right panel of Fig. 6 shows that the two damping coefficients have same temperature dependence and agree within a factor of two. This relationship indicates that 2γ has the same physics origin as a_1. The coefficients, a_1 and 2γ, vary by a factor of 7.1 and 6.9 within the measured temperature range, respectively. We associated these variations due to the temperature dependence of the electrical conductivity of the high purity copper coil. The eddy current coefficient linearly scales with the electrical conductivity [16]. The red curve of Fig. 7 shows the resistivity of RRR = 2000 copper, and it varies by a factor of 6.8 over the same temperature range, which is consistent with the change in a_1 and 2γ. Therefore, the primary source of damping in this system is the eddy current loss in the coils as evidenced by its temperature dependency comparing to a_1.

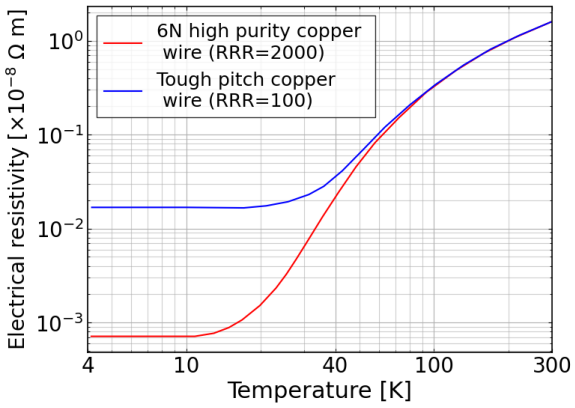

Figure 7: The electrical resistivity of copper as a function of temperature for different RRR values based on [13]. The red curve represents the case of RRR = 2000, and the blue curve represents RRR = 100.

5.2 The mitigation of the rotational instability

We have preliminarily identified that the cause of the damping is eddy currents induced in the coils. To redesign the rotation mechanism and mitigate rotational instability, one effective approach is to adjust the coil parameters, such as the number of turns or the resistivity of the copper wires, to generate larger eddy currents. However, these optimizations can lead to larger heat dissipation in the coil.

Other methods to balance reducing the rotational instability and minimizing heat dissipation include tuning the acceleration parameters to reduce oscillations and applying feedback controls using encoder signals. These approaches could help achieve a more stable rotation mechanism with minimal heat dissipation.

6 Conclusion

We conducted cryogenic rotation tests of the SMB-based rotation mechanism at different coil temperatures. We quantified the rotational instability and investigated the cause of damping in the oscillation of rotational frequency. The result showed that the parameters corresponding to the damping of oscillation and the parameters representing the eddy current loss of the spin-down are the same order and have the similar dependence on the coil temperature, so the main cause of damping is thought to be the eddy current loss induced in the high-purity copper coils. We will refine the procedure of analyses, which are reconstruction of rotational frequency and estimation of each parameter by fitting the oscillation. Our future plan is to mitigate the rotational instability towards practical application as polarimeters.

Acknowledgement

This work was supported by JSPS KAKENHI Grant Number JP23H00107. This work was performed in part at the Center for Data-Driven Discovery, Kavli IPMU (WPI). The Kavli IPMU is supported by World Premier International Research Center Initiative (WPI Initiative), MEXT, Japan.

References

[1] J.R.Hull, Superconducting bearings, 2000 *Superconductor Science and Technology* **13** (2) R1

[2] H.J. Bornemann, T. Ritter, C. Urban, O. paitsev, K. peber and H. Rietschel, Low friction in a flywheel system pith passive superconducting magnetic bearings, 1994 *Applied Superconductivity* **2** (7) 439-447

[3] J.R.Hull, T.M.Mulcahp, K.L.Uherka, R.A.Erck and R.G.Abboud, Flywheel energy storage using superconducting magnetic bearings, 1994 *Applied Superconductivity* **2** (7) 449-455

[4] J.R.Hull and T.M.Mulcahy, Gravimeter using high-temperature superconducting bearing, 1999 *IEEE Transactions on Applied Superconductivity* **9** (2) 390-393

[5] E.Lee, K.B.Ma, T.L.Wilson and W.Chu, Characterization of superconducting bearings for lunar telescopes, 1999 *IEEE Transactions on Applied Superconductivity* **9** (2) 911-915

[6] W.Yang, Y.Ji, M.Ye and H.Tang, A micro-force measurement system based on high-temperature superconducting magnetic levitation, 2019 *Measurement Science and Technology* **30** (12) 125020

[7] S.Hanany, T.Matsumura, B.L.Johnson, T.J.Jones, J.R.Hull and K.B.Ma, A cosmic microwave background radiation polarimeter using superconducting bearings, 2003 *IEEE Transactions on Applied Superconductivity* **13** 2128-2133

[8] A.Kusaka et al., Modulation of cosmic microwave background polarization with a warm rapidly rotating half-wave plate on the Atacama B-Mode Search instrument, 2014 *Review of Scientific Instruments* **85** (2) 024501

[9] A.M.Aboobaker et al., The EBEX Balloon-borne Experiment—Optics, Receiver, and Polarimetry, 2018 *The Astrophysical Journal Supplement Series* **239** (1) 7

[10] C.A.Hill et al., A cryogenic continuously rotating half-wave plate mechanism for the POLARBEAR-2b cosmic microwave background receiver, 2020 *Rev. Sci. Instrum.* **91** (12) 124503

[11] K.Yamada et al., The Simons Observatory: Cryogenic half wave plate rotation mechanism for the small aperture telescopes, 2024 *Rev. Sci. Instrum.* **95** (2) 024504

[12] R.Takaku et al., Development status of the polarization modulator using 330 mm diameter sapphire-based achromatic half-wave plate for LiteBIRD, 2024 *Proc. SPIE PC13102, Millimeter, Submillimeter, and Far-Infrared Detectors and Instrumentation for Astronomy XII* **PC13102** PC131021D

[13] C.A.Thompson, W.M.Manganaro and F.R.Fickett, Cryogenic Properties of Copper, 1990

[14] R.Akizawa et al., Experimental Energy Loss Analysis of the SMB-Based Rotation Mechanism Below 10 K, 2025 *IEEE Transactions on Applied Superconductivity* **35** (5) 1-5

[15] M. Zeisberger and W. Gawalek, Losses in magnetic bearings, 1998 *Materials Science and Engineering: B* **53** (1) 193-197

[16] P.L.Richards and M.Tinkham, Magnetic Suspension and Propulsion Systems for High-Speed Transportation, 1972 *Journal of Applied Physics* **43** (6) 2680-2691